Engineering Science and Technology, an International Journal 55 (2024) 101743

Contents lists available at ScienceDirect

Engineering Science and Technology, an International Journal

journal homepage: www.elsevier.com/locate/jestch

Full Length Article

Predictive modelling of residual stress in turning of hard materials using radial basis function network enhanced with principal component analysis

Adalto Farias [a,*,1], Nelson W. Paschoalinoto [b,2], Ed C. Bordinassi [b,3], Fabrizio Leonardi [a,4], Sérgio Delijaicov [a,5]

[a] University Center FEI– Ignatian Educational Foundation, Av. Humberto de Alencar Castelo Branco, 3972-B, Assunção, São Bernardo do Campo, São Paulo 09850-901, Brazil

[b] University Center of Mauá Institute of Technology, Praça Mauá 1, São Caetano do Sul, São Paulo 09580-900, Brazil

ARTICLE INFO

Keywords:
Residual stress
Prediction
Hard turning
Machine learning
Radial basis function
Principal component analysis

ABSTRACT

This study proposes a hybrid machine learning (ML) model that combines a radial basis function network (RBFN) with principal component analysis (PCA) to predict residual stress (RS) in the machining process. Higher temperatures and plastic deformation can generate RS conditions in the machining of hard materials, significantly influencing the quality of machined parts, particularly their surface integrity. It is crucial to evaluate and guarantee machining conditions that ensure reliable surface integrity that yields compressive RS conditions. Incorrect parameter settings can lead to poor surface quality, resulting in tensile RS conditions that impact both the quality and lifetime of manufactured products. The methodology involved experimental machining trials for data acquisition, with conditions selected for hard material machining tests conducted using a computer numeric control (CNC) lathe under dry cutting conditions. The cutting force components were measured, and RS was evaluated using X-ray diffraction. A total of 60 trials were conducted. Data preprocessing, including normalization and removal of outliers, was executed before constructing the ML algorithm, leaving 59 valid tests for model training and testing. Separate datasets for training (70 % of the data) and testing (30 %) were randomly selected from the valid experimental tests. PCA enhanced the RBFN model's generalization by reducing data dimensionality and providing the hidden units parameter. The eigenvectors obtained through PCA served as an efficient initial reference for RBF centroids, highlighting principal directions of variation. The PCA-RBFN model, using a multiquadric radial function, exhibited robust performance in capturing underlying patterns during training and demonstrated balanced results in the tests. In the PCA-RBFN model training stage, it exhibited a coefficient of determination (R^2) of 76.66 %, a mean average error (MAE) of 72.15 MPa, and a root mean square error (RMSE) of 84.94 MPa. In the testing stage, the model showed increased metrics, indicating its ability to predict RS values accurately, with an R^2 of 80.54 %, MAE of 51.25 MPa, and RMSE of 70.36 MPa. The evaluation between the training and testing stages highlighted the model's coherence in performance, demonstrating its ability to generalize well to new data. A second comparative analysis was conducted with a conventional RBFN approach using stochastic method for centroid determination. The hybrid PCA-RBFN method exhibited lower computational effort, requiring only three iterations compared to 221,923 iterations in the conventional approach. Despite the conventional approach yielding better metrics in the training stage, it exhibited signs of overfitting, a common concern in machine learning models. The hybrid PCA-RBFN consistently outperformed it regarding generalization and fit during testing. The proposed methodology holds practical implications for the manufacturing industry, allowing the integration of a pre-trained predictive model into machine controllers or smart sensors. The hybrid PCA-RBFN's computationally lightweight approach also supports incorporating real-

* Corresponding author.
E-mail address: afarias@fei.edu.br (A. Farias).
[1] https://orcid.org/0000-0002-6780-2804.
[2] https://orcid.org/0000-0003-2094-6031.
[3] https://orcid.org/0000-0002-3915-3077.
[4] https://orcid.org/0000-0001-8056-7645.
[5] https://orcid.org/0000-0001-5621-9536.

https://doi.org/10.1016/j.jestch.2024.101743
Received 20 March 2024; Received in revised form 3 June 2024; Accepted 11 June 2024
Available online 18 June 2024

time adaptive algorithms into production systems, enabling continuous real-time adjustments to the model factors and weights, thereby improving automated control.

1. Introduction

Integrating intelligent systems, such as Artificial Intelligence (AI) or Machine Learning (ML) systems along with Internet of Things (IoT) or as a decentralized production system (DPS), into the manufacturing sector has emerged as a transformative approach, offering solutions to long-standing challenges and making the production systems more flexible and collaborative, [1]. Many intelligent systems can model and optimize processes in industry, the machining process is one candidate for intelligent systems. According to C. Li et al. [2] manufacturing companies of all sizes worldwide continue to develop in the direction of intelligence, and formulating a reasonable and efficient digital strategy will steadily boost their competitive advantages.

The machining process is a method for removing material from a blank workpiece, metallic or not, to achieve a desired form according to a project specification, using a cutting tool, a machine, and dynamic conditions known as cutting parameters or machining parameters. According to Mazid et al. [3] understanding the appropriate machining parameters that could produce the best surface roughness, geometric accuracy, and lower sublayer residual stresses crucial in the metal machining area. If the parameters are set incorrectly, the surface quality can be coarse, affecting the quality and lifetime of manufactured products.

The metal machining manufacturing process involves temperature variation, which can modify the mechanical performance and microstructure of materials due to the complex thermal history [4], so predicting the component performance is essential for the manufacturing industry, especially in the area of aerospace, automotive, and machinery [5].

Despite the existence of various advanced techniques for temperature reduction in machining processes [6,7], which can be employed to lower the temperature and enhance sustainability in terms of energy usage and tool wear, higher temperatures and plastic deformation occurring at the cutting edge in the tool-workpiece-chip interface can lead to residual stress conditions. The quality of machined parts is often characterized by their surface integrity, with residual stress being identified as one of the most critical factors, [8].

Khoshaim et al. [9] also affirm that the induced residual stresses substantially impact the quality and lifetime of products. Geng et al. [10] cites that residual stresses and distortion can critically degrade components' structural integrity and performance. G. Li et al. [11] emphasize considering residual stresses in manufacturing parts. They point out that machining-induced residual stresses can significantly impact the distortion of parts, as noted by Akhtar et al. [8]. Therefore, controlling these residual stresses is crucial for ensuring the quality of the manufactured parts.

The formation of residual stress depends on the thermal and mechanical effects during manufacturing [12], and understanding the relationship between residual stress and process parameters is essential to produce better products, especially for critical applications parts, [13]. A comprehensive understanding of residual stress mechanisms can be found in [8]. Compressive residual stresses benefit parts lifetime, while tensile residual stresses are detrimental [14]. Compressive residual stress can improve topological parts' wear resistance and inhibit fatigue crack propagation [15].

Analytical approaches solely cannot cover the complexity of the machining factors that influence residual stress surface conditions since they need specific in-depth knowledge of plastification, phase transformations, microstructural changes, and their influencing factors [13,16], neither finite element simulations, which are often too time-consuming [17]. According to Alamaniotis et al. [18] experimental techniques to measure residual stress distribution come at a high financial cost and cannot be deployed in situ. Also, they can be a semi-destructive technique, so predictive monitoring supports the prior scheduling of critical component maintenance. It contributes significantly to attaining a safe yet economical operation and management of complex energy systems.

The prevailing approach is to establish correlations between this residual stress and other more accessible process-related variables, whether inputs or outputs. These variables are often chosen due to their ease of control, the feasibility of simulating them, or straightforwardness in measurement. Researchers use these established relationships to create more reliable methods for predicting residual stress. Khoshaim et al. [9] investigated the effects of the machining process factors (cutting speed, cutting depth and feed) on the induced residual stresses of machined surfaces during turning of pure iron disks and developed hybrid artificial intelligence models to model the residual stresses generation in both of circumferential and radial directions. The models consisted of a conventional artificial neural network ANN model and hybrid ANN incorporated with particle swarm optimization and flower pollination algorithm. The developed hybrid models had better prediction accuracy compared with that of the standalone ANN model and hybrid machine learning approach outperforms the other state-of-the-art approaches when only a small amount of supervised data is available [19].

AI has been applied for a long time in product manufacturing from machine monitoring and controlling [20,21] to process planning [22], and several approaches have been studied to help predicting residual stress in order to avoid the need for measurements. Rajaguru et al. [23] during orthogonal cutting of super duplex stainless steel, predicted the residual stresses using Coupled Eulerian-Lagrangian (CEL) formulation. Sánchez-López et al. [24] proposed the use of response surface methodology (RSM) and the variant of multiquadratic radial basis function (RBF) for surface roughness modeling. Chu et al. [25] studied the roundness of grinding workpiece prediction through the vibration signals using the Gaussian radial kernel function online during the process. IoT and AI are enabling key technologies [2] to data-driven optimization which eliminates the necessity of resource driven mathematical or simulation paradigms for the manufacturing process optimization, [26]. Schott et al. [16] demonstrated the capabilities of data-driven modeling approaches for predicting surface residual stress using Takagi-Sugeno multi-models compared to multiple linear regression as a baseline approach. According to Schajer et al. [27] residual stresses can be introduced throughout all manufacturing stages and vary during component life. They are difficult to predict, and their evaluation presents more significant challenges compared to measuring applied stresses due to their hidden nature; there is no need for external loads to their appearance. These challenges include potential physical damage to specimens during measurements, material-specific calibrations, sensitivity to nearby stresses requiring inverse calculations, and high precision demands due to sensitivity to imperfections in measurement procedures and measurement uncertainty estimation, [28].

Salmani Ghanbari and Mahmoudi [29] compared two methods, the k-nearest neighbor (kNN) machine learning and the Kriging model, to interpret and estimate the residual stresses and mechanical properties of aluminum plates, and the results showed that kNN algorithms have a better slightly result than the Kriging model. Mathew et al. [13] compared two methods, (ANN) and fuzzy neural networks (FNN), to predict residual stresses in the welding process of power plant components and demonstrated the potential benefits of implementing neuro-fuzzy systems in predicting residual stresses profiles using experimental data. Alamaniotis et al. [18] implemented probabilistic kernel

machines for predictive monitoring of weld residual stress in energy systems using Gaussian Processes (GP) equipped with various kernels for the estimation of weld residual stress profiles of stainless-steel pipe welds. The GP models were tested on experimentally obtained data of axial and hoop residual stresses, and the results exhibit the ability of GP to predict the weld residual stress profiles accurately.

Elsheikh [30] presented a comprehensive review paper on the applications of ML methods in the friction stir welding manufacturing process field, aiming at predicting the properties of the welded joints, real-time control, tool failure diagnosis, and incorporation of numeric simulations. His main conclusions were that machine learning methods had demonstrated significant potential in modeling various friction stir welding processes across different welding conditions and materials and had surpassed traditional statistical methods like response surface methodology. However, one ML limitation over statistical methods is its marginally increased computational time. In his opinion, it's essential to understand that no single ML model structure is universally optimal for all processes and conditions.

The radial basis function network (RBFN) has been used in many applications for nonlinear mappings between inputs and outputs in nonlinear control systems [31,32]. It also can determine the relationship between the response and the independent variables, showing the individual importance of variables in the model [33]. According to Fu et al. [34] it can also be used for performance evaluation, real-time forecasting, optimization, and adaptative control. RBFN was also used to predict the thermal error in a feed system of a machine tool by T. Jun Li et al. [35]. Ullah et al [36] describe the use of radial basis function (RBF) for topology optimization, and Banda et al. [37] used RBF to predict the flank wear of Inconel 718 during milling.

Two critical aspects of the accuracy of an RBF network reside in the definition of the number of hidden layer units and its values of centroids or kernels. Some works have explored alternatives for the systematic determination of these parameters. In general, there are two types of approaches: trial-and-error iterations on random arbitrary values accounting in an objective minimizing function [38–40] and hybrid approaches [41].

Hybrid approaches have been applied to increase the precision of RBFN methodology. Lin & Lian [31] studied the hybrid self-organizing fuzzy controller (SOFC) and RBFN controller to keep the cutting forces constant while turning in real-time, which RBFN got better results than the SOFC. Mazid et al. [3] concluded that support vector machine algorithm with radial basis function kernel (SVM-RBF) appears to be highly suitable for studying machining operations of Ti-6Al-4V alloy due to achieving the least root mean square error (RMSE) most times compared to the other ML classifiers in predicting the surface roughness. Soepangkat et al. [42] employed a hybrid multi-response optimization approach for drilling carbon fiber reinforced polymer (CFRP) by utilizing back propagation neural network-particle swarm optimization (BPNN-PSO). The results of the confirmation experiment revealed that the integration of BPNN and PSO effectively predicted and improved the multi-performance characteristics with a high degree of accuracy.

Praga-Alejo et al. [33] adapted the Ridge method for the radial basis function to define the hidden layer unit's inputs. The conclusion was that the redesigned radial basis function improves model accuracy when combined with the Ridge method. Phate & Toney [43] used dimensional analysis (DA) and artificial neural network (ANN) to evaluate surface roughness and material removal rate of Al 2124 SiCp Metal Matrix Composite (MMC) in wire electrical discharge machining (WEDM). They correlated parameters such as pulse on time, pulse off time, wire feed rate, current, voltage, thermal conductivity, coefficient of thermal expansion, density, and wire tension. Both DA and ANN models accurately predicted surface roughness and material removal rate, as indicated by correlation coefficient values.

PCA is a technique known for its ability to significantly reduce the number of influential variables in modeling, especially when there is the possibility of existing high dimension and correlated nature in the analyzed data [44–46]. PCA can find the principal sources of variability in the space of the measured variables, thus reducing the dimensionality of the original space to fit into a new one with the minimum number of uncorrelated variables required to explain the process trends. This reduction is done by searching linear combinations between the measured variables [45].

The work outlined in this paper employs a machine learning radial basis function network (RBFN) to predict the residual stress condition of surface machined components as a function of the process parameters and the measured cutting forces. The search for the ideal number of hidden layer units and reference values for the centroids/kernels of an RBFA is often computationally expensive, preventing the development of more compact models that can be directly incorporated into the control of a machine or a measurement sensor. A combined approach, or hybrid proposal, was used for this paper to create a systematic procedure to determine the number of hidden layer units and its values of centroids/kernels. The principal component analysis (PCA) technique was used to determine the number of hidden layer units and its kernels or centroids parameters for the RBFN predicting surface residual stress.

The structure of this work can be understood from Fig. 1, which displays the general flowchart of the employed methodology. The flowchart outlines the four main phases of the research: (a) Experimental machining trials for data acquisition on machining forces and measurement of residual stress in the machined parts. (b) Data preprocessing involves normalization and identification/removal of outliers present in the input data. (c) Construction of the machine learning (ML) algorithm, utilizing PCA for data dimensionality reduction, and determining the number and values for the hidden layer units of the RBFN. (d) Evaluation of the PCA-RBFN's performance on training data, with separate validation data not used during training and with stochastic (or conventional) method of modeling RBFN. The final ML algorithm's performance was assessed using R-square (R^2), Adjusted R-square ($R^2_{adjusted}$), Predicted R-square ($R^2_{predict}$), Mean Absolute Error (MAE) methodologies, and Root Mean Square Error (RMSE) [47].

This work aimed to predict the residual stress in turning of hard materials based on experimental measurement using RBFN enhanced with PCA machine learning algorithm as a function of the process parameters and the measured cutting forces. A significant practical implication of this study is the potential for predictive monitoring of residual stress in *loco* during the production stages. The low computational time required for the algorithm methodology using PCA and RBFN, combined with the straightforward output of the RBFN as a regression equation, makes its integration into a machine controller or sensor embedding quite feasible. Such integration offers two possible routes: (i) the development of automated quality control/traceability techniques, benefiting from the system's simplicity, and (ii) enabling timely and cost-effective replacements of critical system component measurements, thanks to accurate predictions of residual stress.

In short, incorporating the predictive model into the production system can help optimize the turning process in real time. By providing feedback to the manufacturing system, adjustments can be made to process parameters, resulting in increased efficiency, reduced energy consumption, and improved overall performance.

2. Dataset generation

2.1. Machining tests with experimental measurements

All test samples for the experimental trials were made of the steel alloy AISI 52100, commonly used for mechanical bearing components. These samples had a cylindrical geometry with a diameter of 25.4 mm and a total length of 80 mm, as shown in Fig. 2(a). After being quenched and tempered, the average hardness of the samples was measured to be 58.5 ± 2 HRC. The chemical composition of the steel used for the tests is listed in Table 1.

All machining tests were conducted using a Lathe Centur 30D from

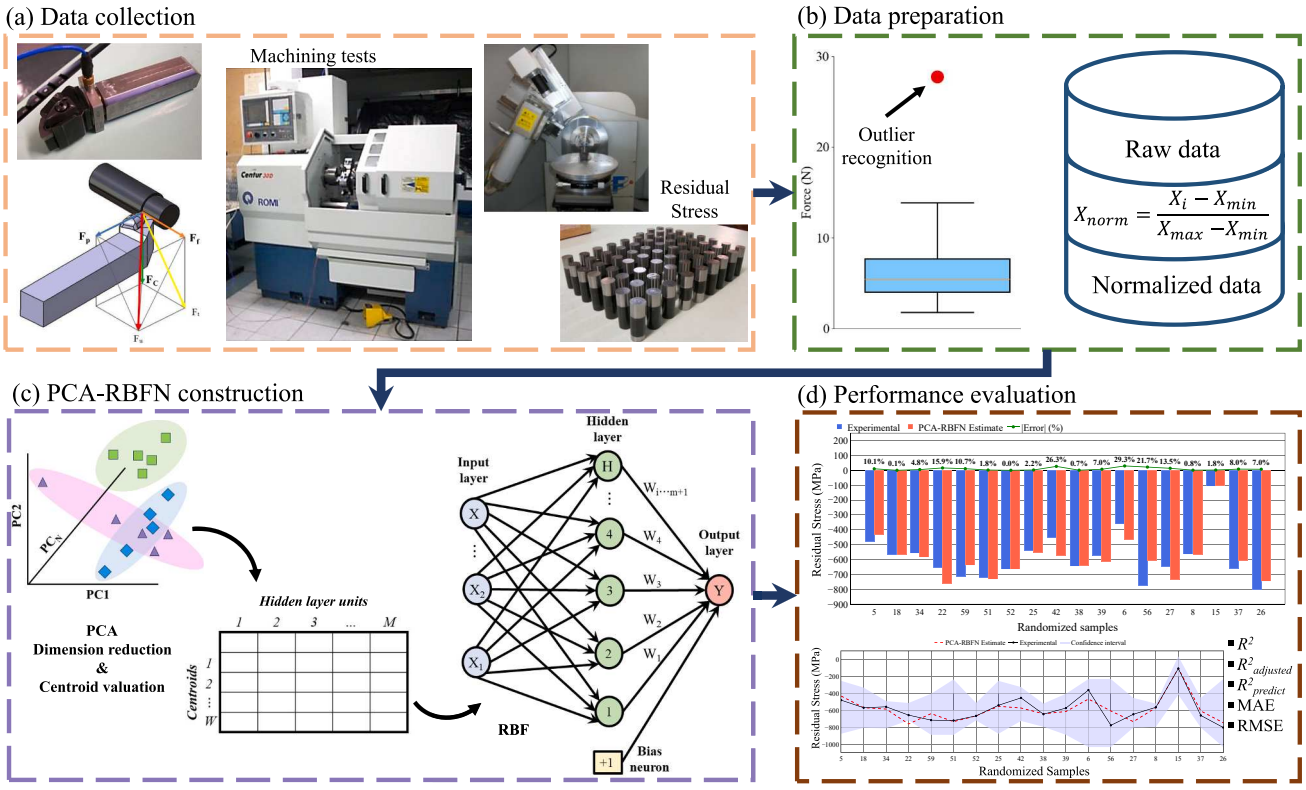

Fig. 1. General flowchart of the methodology employed.

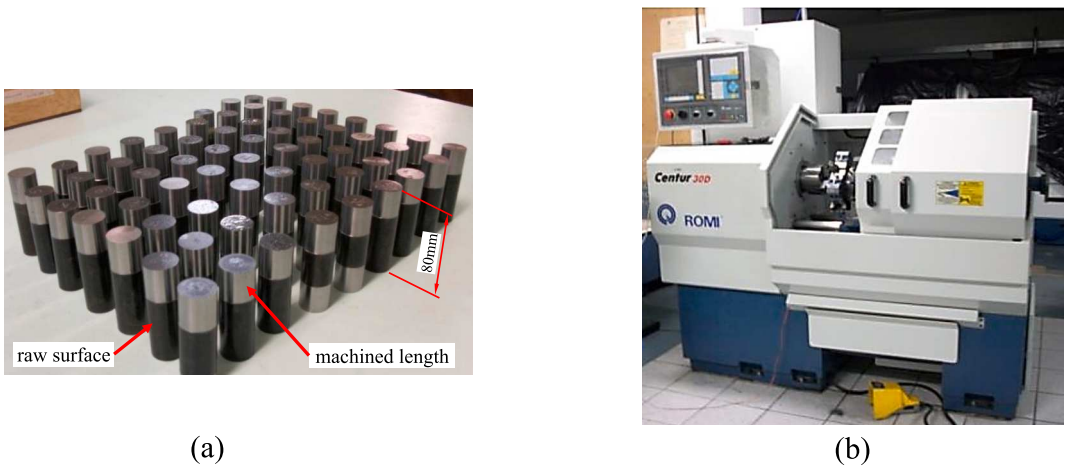

Fig. 2. (a) Steel samples for the machining tests, (b) Lathe Centur 30D applied in the experimental tests.

Table 1
Chemical composition of the AISI 52100 steel.

Element	C	Si	Mn	Mo	S	Cr	Ni	Cu	Fe
percentual %	1.18	0.20	0.28	0.028	0.003	1.36	0.091	0.062	Res.

the Romi® manufacturer, Fig. 2(b). The machining was done under dry-cutting conditions, and each sample had a machined length of 30 mm.

The turning tool consisted of a holder and its cutting inserts, as shown in Fig. 3(a). The holder's specification was DWLNR 2020 M08, and during machining tests, the cutting force components were measured using a calibrated force transducer, model PCB-260A02 from the company PCB Piezotronics, coupled to the insert holder, as shown in Fig. 3(a). The measured cutting components were the cutting force (F_C) in the cutting speed (V_C) direction, feed force (F_f) in the feed rate (f) direction, and penetration force (F_P) in the cutting depth direction. Fig. 3 (b) presents the measurement diagram, showing the directions of the measurements when the cutting tool edge engages with the sample

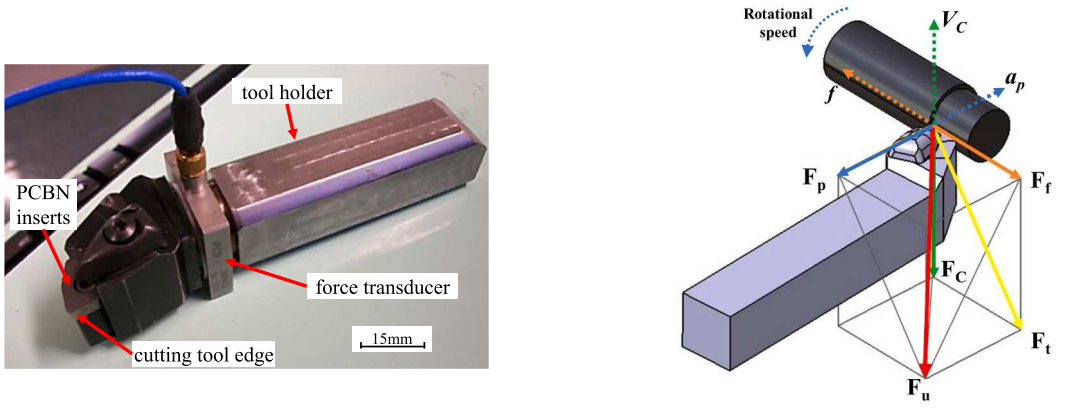

Fig. 3. (a) Cutting tool assembly with force transducer coupled to the holder, (b) diagram of force component measurements.

surface during cutting.

Data acquisition of the force measurements during machining was conducted using a QuantumX MX840B signal conditioner. The software Catman® from HBM company was used. A frequency of 200 Hz was adopted for the data signal acquisition by configuration.

Two different types of PCBN (polycrystalline cubic boron nitride) cutting inserts were used for the experiments and all the tool components were manufactured by Sandvik®. The PCBN cutting inserts were classified in this work as Type 1 (code WNGA 08 04 08 S01030 7025), Fig. 4(a), and Type 2 (code WNGA 08 04 04T01020 7525), Fig. 4(b). The shape of the cutting tool inserts allows for the use of six edges to perform the tests, and both its sides (top and bottom) can be used. The primary differences between the two insert types are the tool tip radius (r_ε) being 0.8 mm for Type 1 and 0.4 mm for Type 2, as well as the geometric design of the cutting tool edge, as presented in Fig. 4(a) and Fig. 4(b). Type 1 features a 30 degrees chamfer with a honed rounded (h_R) edge with an approximate radius of 0.01 mm, and Type 2 features a 20 degrees chamfer with sharp edges.

A model XRD-7000 diffractometer from Shimadzu was used to measure the surface residual stresses, as shown in Fig. 5(a). The direction of the residual stress measurement was circumferential (on the cylindrical surface of the specimen), as depicted in Fig. 5(b). Angles of 0°, 15°, 30°, and 45° were adopted as measurement standards, and Fig. 5 (b) displays one of the residual stress tests being conducted. The $sin^2\psi$ method was employed to determine the surface residual stress.

The machining tests were conducted following a full factorial design of three input factors in two levels with the addition of two central points. The three independent variables were cutting speed (V_C) in meters per minute (m/min), feed rate (f) in millimeters per revolution (mm/rev) and cutting depth (a_P) in millimeters (mm).

The cutting data for the independent variables under consideration are presented in Table 2, all the values were selected from the tooling manufacturer's catalog to extrapolate finishing conditions.

The dependent variables that were observed and measured were the cutting force (F_C) in Newtons (N), feed rate force (F_f) in N, penetration force (F_P) in N, and residual stress (RS) in mega Pascal (MPa).

The factorial planning generated a ten runs combination of parameters for the machining tests. Six replicates were conducted for the tests resulting in a total of sixty runs. The resulting configuration is shown in Table 3.

2.2. Experimental results and discussion

Table 3 presents the collected data from all the 60 runs, randomly conducted, during the experimental machining tests. For each numbered test (#), the associated cutting data: cutting speed (V_C) in m/min, feed (f) in mm/rev, cutting depth (a_p) in mm, tool type (tp), and tip radius (r_ε) in mm. The machining force components measured in the tests are reported as cutting force (F_C) in N, feed force (F_f) in N, and thrust/penetration force (F_P) in N. Residual stress (RS) was measured in MPa.

To visualize and primarily understand the influence of the independent cutting condition variables on the resulting residual stress values from the tests, a main effect plot was used as an initial visualization strategy to evaluate trends, potential correlations, and interactions for the mean residual stress. Fig. 6(a), Fig. 6(b), and Fig. 6(c) present the main effect plot for the mean residual stress values against V_C, f, and a_P. The error bars represent a 95 % confidence interval (CI). The overall standard deviation estimates for the variables acquired

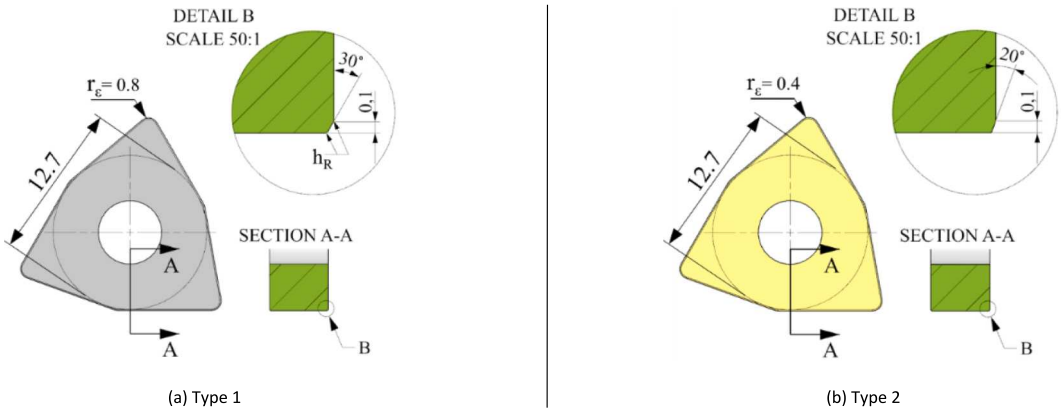

Fig. 4. PCBN insert shape and cutting tool edge geometry configuration (a) Type 1 (b) Type 2, linear dimension in mm.

(a) (b)

Fig. 5. (a) Diffractometer model XRD-7000, (b) circumferential direction sample measurement.

Table 2
Factorial planning applied in the machining for each tool cutting insert geometry.

	Low	Central	High
V_C (m/min)	200	225	250
f (mm/rev)	0.06	0.08	0.1
a_P (mm)	0.05	0.1	0.15

during the tests, F_f, F_C, F_P, and RS, are presented in Table 4. These values represent the uncertainties inherent in the measurement data, which could potentially influence the final experimental analysis and modeling results.

In general, Fig. 6 demonstrates a compressive RS condition consistent with previous research evaluating turning conditions in materials with similar hardness levels [12,16]. A nonlinear behavior of the means RS for the three independent variables can be observed in Fig. 6(a) to Fig. 6(c) under central planning values test conditions.

In Fig. 7(a) and Fig. 7(b), it is possible to observe the main effect of tool type and tool tip radius on RS means, where the most compressive conditions are achieved with Type 1 insert and a larger tool tip radius of 0.8 mm. Furthermore, an apparent inverse correlation between tool type and r_ε is noticeable in relation to the order of magnitude and behavior of the RS averages. Wittich et al. [48] and Schott et al. [16] also discussed the nonlinearity condition of RS in cutting conditions. They emphasized that such manufacturing processes might be a promising application area for computational intelligence methods due to their nonlinear characteristics and causal relationships that are not yet fully understood.

3. Machine learning neural network model construction

During the machine learning modeling phase, a combined approach of RBF and PCA was employed to optimize data representativeness and enhance model efficiency. PCA was used to transform the original dataset into a feature space with reduced dimensions (or input factors), preserving as much variance as possible. Subsequently, the RBF network was used to construct a prediction regression model. RBF neurons use radial functions, the centroids of which, in this context, were derived from the principal components produced by PCA. This combination aimed to achieve a robust and efficient model. The overall machine learning neural network model architecture is presented in Fig. 8. All the routines and modeling were implemented in Python-Version 3.7.6.

Individual RBF neural networks and individual PCA techniques have been applied in various research domains and are well-documented and thoroughly explained [3,33,44,45,49–52]. Consequently, this work will focus only on the specific implementation of the machine learning model, detailing its steps, highlighting critical passages, discussing relevant topics, and presenting only the essential points for its proper functioning.

The collected raw data and machining forces for the proposed model were statistically analyzed in search of highly discrepant (outliers) values that could cause inconvenient bias in the model prediction results. Each column of Table 3 containing the experimental measurements of machining force (F_C, F_f, and F_P) was checked using the Interquartile Range (IQR) outlier recognition routine established in Eq. (1) [53–56].

$$outlier = \text{True} \Leftrightarrow \begin{cases} F_i \leq Q1 - 2{\cdot}IQR \\ F_i \geq Q3 - 2{\cdot}IQR \end{cases} \quad (1)$$

In Eq. (1), F_i represents the individual value of the machining force component for test #i, Q1 denotes the first quartile, corresponding to the 25th percentile, Q3 represents the third quartile, 75th percentile, and IQR stands for the interquartile range between Q3 and Q1. This routine is designed to identify data points that fall significantly below the lower bound or exceed the upper bound. This approach is usually used for outlier detection [56] and doesn't rely on the assumption of a normal distribution. In cases where the result was positive (outlier = True), regardless of the force component under analysis, the respective test and its results were discarded.

Fig. 9 presents the result of the box-plot construction from Eq. (1) following the outlier removal process for F_f, F_C, and F_P. In the case of Fig. 9(a) and Fig. 9(b), it is possible to note the existence of outlier test #48, which is highlighted in red. In Fig. 9(a), the F_f value of test #48 is shown to be above the maximum limit indicated by Eq. (1), approximately double the maximum limit, thus being considered an outlier. Similarly, in Fig. 9(b), the F_C value of test #48 is slightly above the maximum indicated by Eq. (1), also qualifying it as an outlier. As a result, test #48 was removed from the dataset due to its deviation from the established condition, leaving the dataset with 59 valid tests.

For the ML training stage, 41 samples were randomly selected from the 59 valid tests, constituting approximately 70 % of the available data. In contrast, for the ML testing stage (model validating), the remaining 18 samples were used, corresponding to about 30 % of the available data.

In Fig. 10(a), it is possible to see the plotting of the experimental machining force components for the 41 training stage samples, measured for each of the samples during the experimental run, along with the RS evaluated later, offline in the diffractometer. Fig. 10(b) presents the experimental machining force components and RS for the 18 samples for the model validation. The samples in Fig. 10 are

Table 3
Collected data for all runs (#).

#	V_C	f	a_p	r_ε	tp	F_f	F_C	F_P	RS	#	V_C	f	a_p	r_ε	tp	F_f	F_C	F_P	RS
	m/min	**mm/rev**	**mm**	**mm**		**N**	**N**	**N**	**MPa**		**m/min**	**mm/rev**	**mm**	**mm**		**N**	**N**	**N**	**MPa**
1	200	0.06	0.05	0.8	1	2.13	7.64	35.0	−440	**31**	200	0.06	0.05	0.8	1	3.73	9.95	45.0	−398
2	250	0.06	0.05	0.8	1	2.84	9.6	41.43	−565	**32**	250	0.06	0.05	0.8	1	3.2	9.24	45.0	−576
3	200	0.1	0.05	0.8	1	1.78	8.18	40.71	−242	**33**	200	0.1	0.05	0.8	1	3.91	13.15	55.0	−454
4	250	0.1	0.05	0.8	1	2.84	9.24	45.71	−614	**34**	250	0.1	0.05	0.8	1	7.82	16.53	53.57	−558
5	200	0.06	0.15	0.8	1	5.33	13.69	59.28	−480	**35**	200	0.06	0.15	0.8	1	7.29	16.71	64.28	−441
6	250	0.06	0.15	0.8	1	5.51	12.98	55.71	−361	**36**	250	0.06	0.15	0.8	1	7.11	16.53	69.28	−588
7	200	0.1	0.15	0.8	1	5.86	17.78	61.43	−500	**37**	200	0.1	0.15	0.8	1	8.0	22.22	87.86	−660
8	250	0.1	0.15	0.8	1	13.87	27.73	75.71	−564	**38**	250	0.1	0.15	0.8	1	12.44	26.13	87.14	−645
9	225	0.08	0.1	0.8	1	4.27	12.44	52.14	−555	**39**	225	0.08	0.1	0.8	1	5.69	16.0	64.28	−573
10	225	0.08	0.1	0.8	1	4.44	12.8	52.86	−510	**40**	225	0.08	0.1	0.8	1	5.33	15.64	64.28	−621
11	200	0.06	0.05	0.4	2	2.31	7.29	43.57	−511	**41**	200	0.06	0.05	0.4	2	3.02	8.71	40.71	−441
12	250	0.06	0.05	0.4	2	2.31	7.47	42.14	−597	**42**	250	0.06	0.05	0.4	2	3.55	10.13	50.0	−453
13	200	0.1	0.05	0.4	2	2.31	9.07	27.86	−96	**43**	200	0.1	0.05	0.4	2	3.38	12.62	45.71	−450
14	250	0.1	0.05	0.4	2	4.62	13.51	39.28	−345	**44**	250	0.1	0.05	0.4	2	3.38	12.62	41.43	−435
15	200	0.06	0.15	0.4	2	4.27	12.27	37.14	−107	**45**	200	0.06	0.15	0.4	2	6.22	16.0	52.86	−270
16	250	0.06	0.15	0.4	2	4.08	12.09	37.86	−175	**46**	250	0.06	0.15	0.4	2	5.33	14.75	47.14	−217
17	200	0.1	0.15	0.4	2	12.27	25.42	78.57	−639	**47**	200	0.1	0.15	0.4	2	7.11	20.27	85.0	−444
18	250	0.1	0.15	0.4	2	7.64	21.51	81.43	−569	***48***	*250*	*0.1*	*0.15*	*0.4*	*2*	*27.73*	*32.53*	*103.57*	*−516*
19	225	0.08	0.1	0.4	2	5.33	14.75	65.71	−690	**49**	225	0.08	0.1	0.4	2	5.51	14.4	70.71	−545
20	225	0.08	0.1	0.4	2	4.44	13.51	59.28	−666	**50**	225	0.08	0.1	0.4	2	5.33	15.11	65.71	−410
21	200	0.06	0.05	0.8	1	6.22	13.87	72.14	−690	**51**	200	0.06	0.05	0.8	1	5.51	12.8	65.0	−720
22	250	0.06	0.05	0.8	1	5.69	13.15	67.14	−656	**52**	250	0.06	0.05	0.8	1	4.44	10.84	55.71	−665
23	200	0.1	0.05	0.8	1	5.33	15.64	74.28	−680	**53**	200	0.1	0.05	0.8	1	3.73	12.09	63.57	−754
24	250	0.1	0.05	0.8	1	4.62	14.22	67.86	−693	**54**	250	0.1	0.05	0.8	1	5.87	12.8	65.71	−742
25	200	0.06	0.15	0.8	1	7.82	18.13	71.43	−540	**55**	200	0.06	0.15	0.8	1	8.71	17.24	83.57	−794
26	250	0.06	0.15	0.8	1	10.13	19.02	96.43	−802	**56**	250	0.06	0.15	0.8	1	7.64	15.82	72.86	−776
27	200	0.1	0.15	0.8	1	11.91	26.67	117.14	−646	**57**	200	0.1	0.15	0.8	1	9.95	23.82	105.0	−706
28	250	0.1	0.15	0.8	1	11.2	25.42	109.28	−698	**58**	250	0.1	0.15	0.8	1	10.13	23.47	106.43	−721
29	225	0.08	0.1	0.8	1	8.18	18.84	91.43	−716	**59**	225	0.08	0.1	0.8	1	5.15	14.22	67.14	−715
30	225	0.08	0.1	0.8	1	8.35	19.2	94.28	−892	**60**	225	0.08	0.1	0.8	1	6.22	15.82	69.28	−588

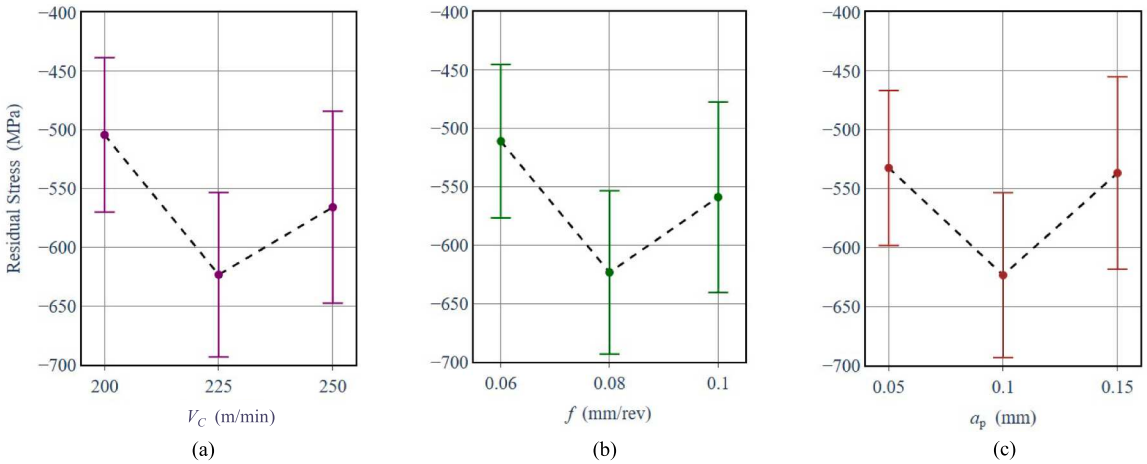

Fig. 6. Main effect plot of means for residual stresses for (a) V_C, (b) f and (c) a_P.

Table 4
Standard deviation estimative for measured variables.

Measured Variable	Standard deviation	Units
RS	120.8	MPa
F_f	1.5	N
F_C	2.2	N
F_P	10.9	N

presented in a randomized sequence, consistent with the format to be utilized in the machine learning model.

From Fig. 10(a) and Fig. 10(b), it is possible to identify an indirect relationship between RS, in MPa on the left scale, and the machining force components measured during the tests, in N on the right scale. Higher values in the forces tend to produce more compressive RS results, as observed in Fig. 10(a) samples #28, 30, 57, 58, for example. Additionally, a direct correlation between the three cutting forces can be identified from the graphs, with F_P presenting the highest modulus and the greatest variation between its extremes (peaks and valleys). Although several works [14,16,23,48,57] have presented methodologies for predicting RS in machining, all have relied solely on process inputs, generally V_C, f, and a_P. None have shown a direct correlation with measuring another quantity, such as machining forces, especially the resulting forces at the tooltip. From the analysis of Fig. 10, it can be observed that the machining force signals, along with the process-dependent variables, can be considered as inputs for RS modeling due to the observed indirect relationship. The use of process output, in this present work, the measurement of machining force signals as a covariate in another output parameter (RS), is a strategy that enhances the model, increasing its robustness.

Before the model construction, the RS values were normalized according to Eq. (2), and two datasets were randomly separated from the original.

$$RS_{iN} = \frac{RS_{iT} - min(RS_T)}{max(RS_T) - min(RS_T)} \tag{2}$$

Where the index i denotes the ith term of RS from Table 3, the index N is the value of the normalized RS, the index T indicates the original value of RS, $\min(RS_T)$ and $\max(RS_T)$ are the minimum, and the maximum values of RS from the table respectively.

3.1. The PCA routine

According to Bishop [58] PCA aims to identify a lower-dimensional space, referred to as the principal subspace. This subspace is characterized by maximizing the variance of the data points when projected orthogonally onto it. An alternative definition of PCA involves

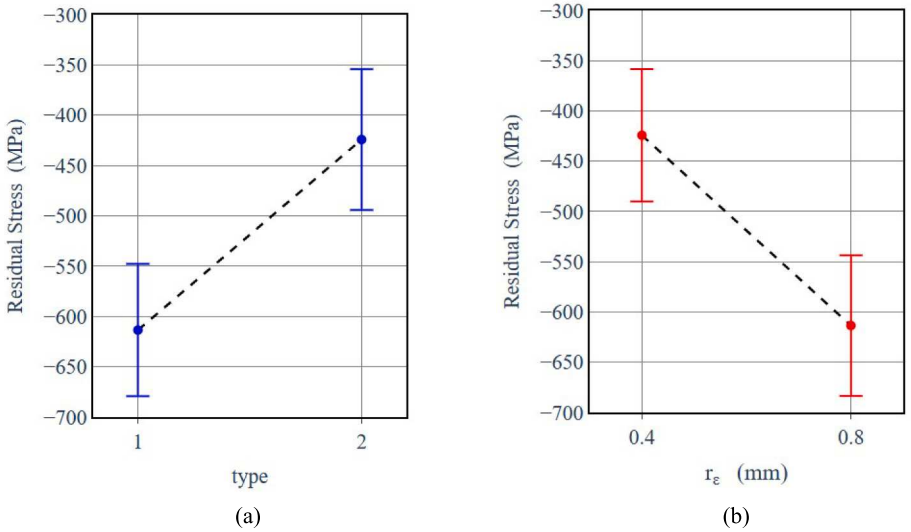

Fig. 7. Main effect plot of means for residual stresses for tool type (a) and tool tip radius (b).

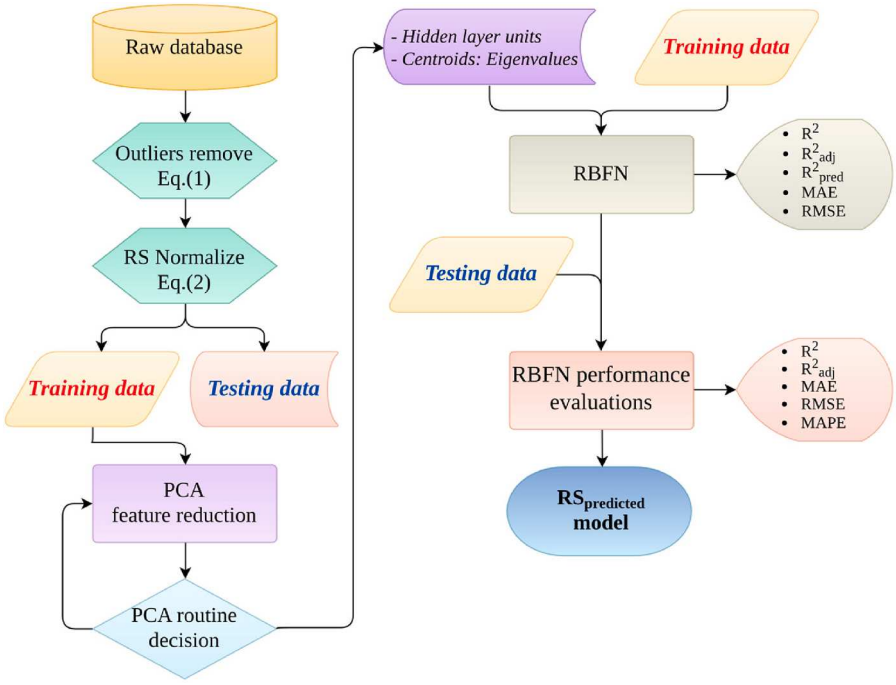

Fig. 8. Machine learning neural network model architecture.

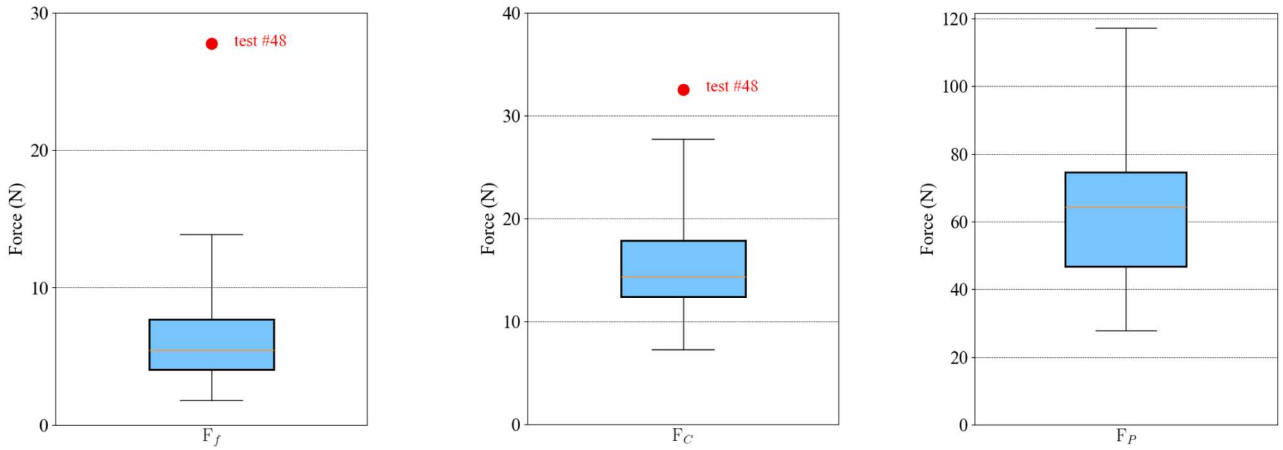

Fig. 9. IQR outlier recognition analysis for (a) F_f, (b) F_C, and (c) F_P. In the case of (a) and (b), the outlier test #48 is represented by a red point. (For interpretation of the references to colour in this figure legend, the reader is referred to the web version of this article.)

minimizing the sum of squares of the projection errors of the data points onto this subspace.

For this work, PCA holds the potential to enhance the generalization of the RBFN model by reducing data dimensionality and providing it the hidden units parameter. PCA eigenvectors serve as a more efficient initial reference for RBF centroids, capturing the principal directions of variation present in the data. In clustering algorithms, as RBF [52], PCA eigenvectors can aid in identifying the underlying structure within the data, facilitating the formation of more coherent clusters. As RBFN relies on kernels/centroids [52], which essentially act as attractors, seeking these attractors aims to find the best combination that minimizes noise/error in the network enhancing efficiency and aiding in the reduction of overfitting in RBFNs.

Utilizing the eigenvectors as centroids the interpretability of the model is increased, since they represent the primary directions of the original data. This can streamline the understanding of how the centroids are distributed within the feature space of a RBFN.

Initially, the model comprised the following eight factors presented in Table 5; besides the input factors, the forces were used in the modeling as covariates for the RS. Residual stress measured in MPa was considered the output for the training step and final performance evaluation.

The use of many factors or features in a model, known as multidimensionality, leads to a possible situation of overfitting the data, meaning that the model performs well with the values used in the training stage but does not perform well in other untrained conditions. PCA can reduce the dimensionality of regression problems, enhance the accuracy estimation, reduce training time and execution time per step, and improve processing speed [59].

Each component's proportion of variance was employed to determine the minimum number of principal components that account for most of the variation in the data. Also, the cumulative proportion of the

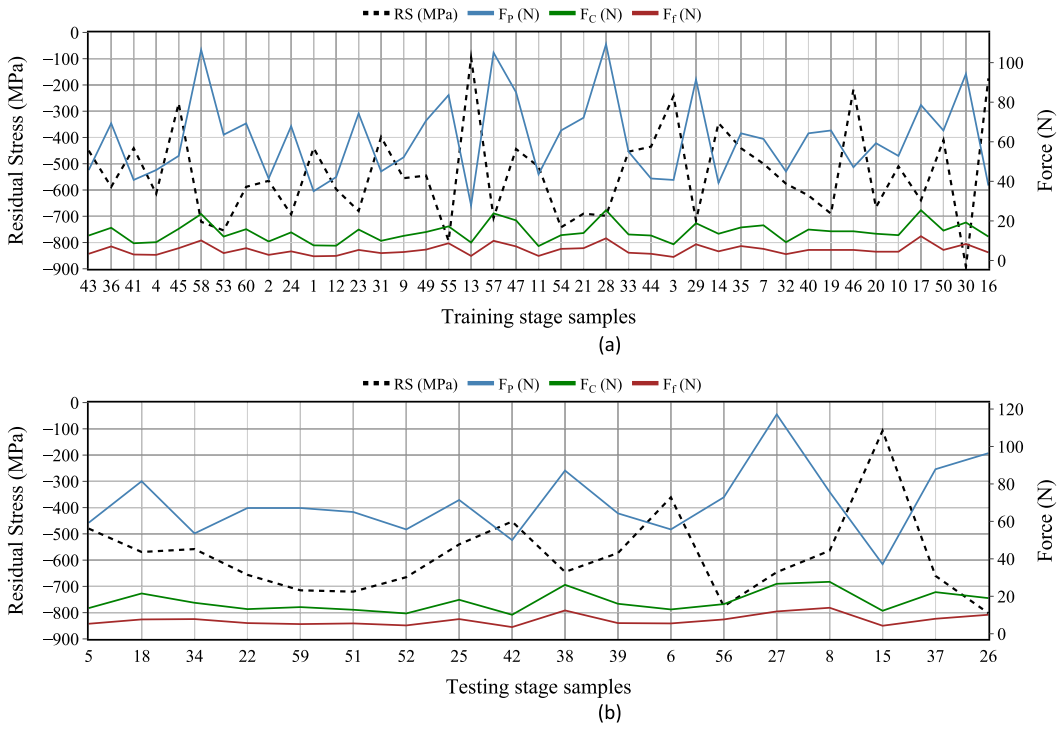

Fig. 10. RS versus cutting force components, (a) 41 samples for the model training, and (b) 18 samples for model validation, both in randomized sequence.

Table 5
Initial factors applied in the machine learning model.

Factor	Description	Unit
V_C	cutting speed	m/min
f	feed	mm/rev
a_P	cutting depth	mm
tp	tool type	—
r_ϵ	tool tip radius	mm
F_f	feed force	N
F_C	cutting force	N
F_P	trust/penetration force	N

variance the principal components explain was used. Individually, principal components that explain an acceptable level of variance equal to or higher than 5 % were kept for the modeling.

Component variance proportion (λp) was determined using Eq. (3), where λ_i indicates the ith eigenvalue, and m represents the number of factors considered for training.

$$\lambda p_i = \frac{\lambda_i}{\sum_{j=1}^{m} \lambda_j}(\%) \tag{3}$$

Fig. 11 presents the PCA routine implemented in Python -Version 3.7.6, where X initially represents the entire set of training factors presented in Table 5. The routine consisted of the main steps: (i) calculating the eigenvalues and eigenvectors for the input factors, (ii) identifying individual components with a variance proportion less than threshold of 5 %, (iii) cross-correlating it with the main factor (X_m) associated with that component through an eigenanalysis of the eigenvectors matrix, (iv) removing the identified factor from the dataset, one factor per iteration, and repeating the routine until all individual components present a variance proportion greater than or equal to the threshold.

Implementing the PCA routine cycle reduced the number of factors from eight to five throughout three iteration cycles. In the order of the routine iteration, the factors eliminated were r_ϵ, F_C, and F_f. Table 6 presents the final result with each principal component's eigenvalues and relative proportions. The five principal components (PC) shown in

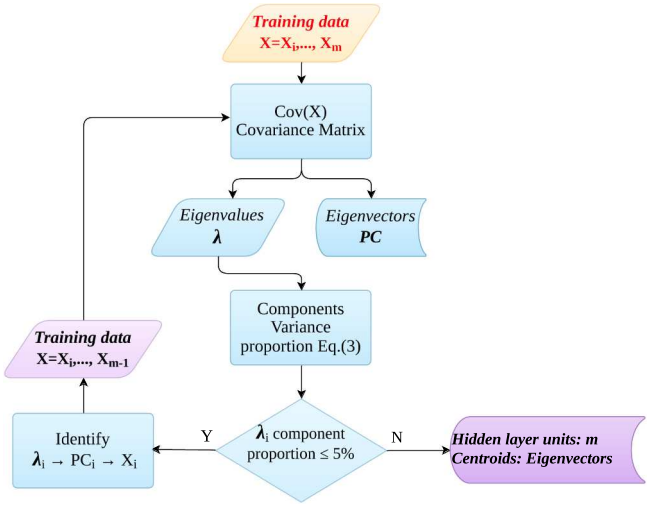

Fig. 11. PCA routine for dimension reduction and centroids valuation.

Table 6
Eigenvalue and relative data of each component.

	λ	λp %	cumulative %
PC1	1.692	33.832	33.832
PC2	1.131	22.613	56.445
PC3	1.002	20.036	76.481
PC4	0.925	18.503	94.984
PC5	0.251	5.016	100.000

Table 6 represent V_C, f, a_P, tp, and F_P, respectively.

The column λ represents the eigenvalue for each principal component identified by the PCA routine. The column λp displays the percentage result of the variance proportion obtained through Eq. (3). The final column represents the cumulative sum of λp. All displayed values

Table 7
Eigenvectors of the PCA.

PC1	PC2	PC3	PC4	PC5
0.015498	−0.109007	−0.971071	−0.211753	0.007672
−0.273248	0.616915	0.070195	−0.670377	−0.300697
−0.531263	−0.615523	0.074857	−0.085990	−0.570870
0.351367	−0.477936	0.215601	−0.705273	0.322838
−0.720692	−0.015522	0.002437	−0.030843	0.692391

are above the 5 % threshold defined by the routine. Table 7 presents the output result with the resultant eigenvectors for each of the principal components of Table 6 to be applied as the centroids for the RBFN implementation.

3.2. RBFN implementation

The radial function chosen for the RBFN model was the normalized multiquadric, Eq. (4), due to its strong convergence rates, such as Gaussian functions [60], during the data interpolation process:

$$\phi(X) = \sqrt{1 + \sigma_i^2 \cdot \|X - Z_i\|^2} \quad i = 1, 2, \ldots, m+1 \tag{4}$$

where X is the input vector matrix with dimension m, Z_i and σ_i are the receptive *i*th neuron centroid and the standard deviation, respectively, and the norm, || - ||, is the m-dimensional Euclidean space. Fig. 12 shows a structural diagram of the RBFN.

The algorithm of the RBFN output is described by Eq. (5). In this equation, $\hat{Y}$ represents the output prediction matrix of the RBFN, where matrix H, Eq. (6), consists of the input data X processed by the radial function ϕ Eq. (4). Matrix W, Eq. (7), represents the weighting factors of the model. The hidden layer H from Fig. 12 and Eq. (5) contain bias neurons (B), which can be implemented by a single hidden unit in the output layer or more, which is always connected. This type of neuron can also be implemented by creating a hidden unit with the value of σ_i is ∞^{-1} [52].

$$\hat{Y} = W \cdot H + B = W \cdot \phi(X) + B \tag{5}$$

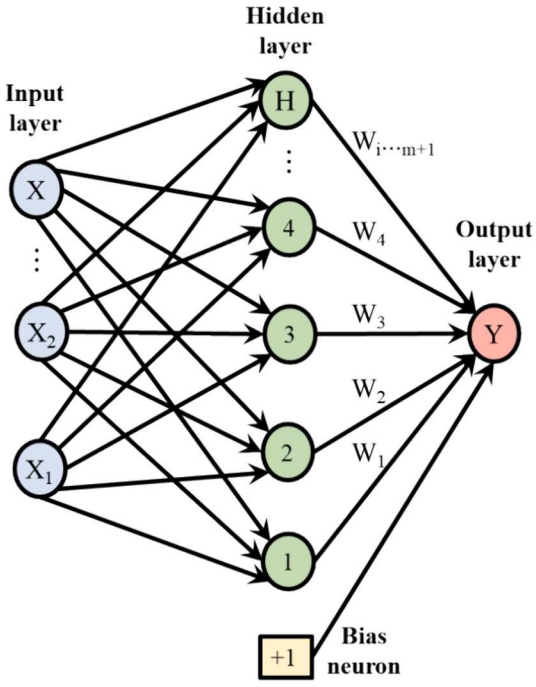

Fig. 12. Radial basis function network diagram.

weight W, which will serve as a reference for the radial function. These are known as hyperparameters, [52]; they are numerical factors that can be used to adjust the final radial expression used to model the problem. For this work, the number of hidden layer units and optimal values were obtained from the PCA routine. The number of hidden layer units was determined to be six ($m + 1$); this includes five layers corresponding to the dimensions of the input factors (m) and an additional layer with a zero-biased centroid heuristically determined. The centroid values are presented in Eq. (9) as the Z matrix of the transposed PCA eigenvectors, added a zero centroid bias vector.

$$Z = Eignv_{PCA}^{T} = \begin{bmatrix} 0 & 0 & 0 & 0 & 0 \\ 0.015498 & -0.273248 & -0.531263 & 0.351367 & -0.720692 \\ -0.109007 & 0.616915 & -0.615523 & -0.477936 & -0.015522 \\ -0.971071 & 0.070195 & 0.074857 & 0.215601 & 0.002437 \\ -0.211753 & -0.670377 & -0.085990 & -0.705273 & -0.030843 \\ 0.007672 & -0.300697 & -0.570870 & 0.322838 & 0.692391 \end{bmatrix} \tag{9}$$

$$H = \begin{bmatrix} \phi_1(x_1) & \ldots & \phi_m(x_1) \\ \vdots & \ddots & \vdots \\ \phi_1(x_i) & \ldots & \phi_m(x_i) \end{bmatrix} \tag{6}$$

$$W = \begin{bmatrix} w_1 \\ \vdots \\ w_m \end{bmatrix} \tag{7}$$

The undefined weighting terms w_i of matrix W are calculated using ordinary least square in accordance with Eq. (8) and are determined based on the experimentally measured values Y of the relative RS:

$$W = H^{+} \cdot Y \tag{8}$$

where matrix H^{+} is the pseudo-inverse [52] of matrix H.

To implement the RBF model, it is necessary to determine the number of hidden layer units H, their optimal centroid values, and the

The standard deviation σ_i in Eq. (4) was computed based on the maximum distance between the centroids Z, and it was held constant across all hidden layer units ($\sigma = \sigma_i$).

The calculation of σ utilized Eq. (10), where d_{max} represents the maximum Euclidean distance among the Z matrix centroids. The calculated value for σ was 0.447214.

$$\sigma = \frac{d_{max}}{\sqrt{2 \cdot (m+1)}} \tag{10}$$

3.3. Training stage performance

The training stage consisted of the 41 random tests selected before the PCA routine optimization. The input factors considered are presented in Table 8, along with the response factor RS, with normalized

Table 8
Input and response factors applied.

factor	description	unit
V_C	cutting speed	m/min
f	feed	mm/rev
a_P	cutting depth	mm
tp	tool type	—
F_P	trust/penetration force	N
response factor		
RS	Residual stress	normalized

values according to Eq. (2), to be used as training condition.

Fig. 13 compares results after the training stage of the PCA-RBFN. It is possible to identify a greater adherence of the model to the experimental points, its behavior, and its ability to capture the underlying patterns within the dataset. Additionally, alongside the experimental data points and the PCA-RBFN estimate, the 95 % confidence interval (CI) is presented, calculated based on the experimental values.

The CI displaying a wide range of variation is likely due to two probable sources, (i) the inherent variation in results among the samples and (ii) the uncertainty intrinsic to the measurement process of RS, as previously discussed and documented in various studies [27,61,62]. According to Fig. 13, only two estimates fall outside the 95 % CI, sample #7 and sample #46. All other estimates are within the specified interval.

The training stage assessment evaluation of the PCA-RBFN model was executed using four metrics: R^2 (coefficient of determination), adjusted R^2 (R^2_{adj}), predicted R^2 (R^2_{pred}), Mean Absolute Error (MAE), and Root Mean Square Error (RMSE) [63]. These metrics assess the model's performance, and a comprehensive application of performance indicators can be found in [30,14].

The following results were drawn from the training stage: R2 demonstrated a value of 76.66 %, indicating the model's capability to explain 76.66 % of the variance in the data. The $R2_{adj}$, which considers the number of predictors, stood at 73.32 %, accounting for model complexity. R^2_{pred}, a measure of the model's predictive accuracy providing an approximately unbiased estimation of the error for models with limited samples [64], achieved a value of 69.37 %, indicating the model's ability to make reliable predictions. Additionally, the MAE was found to be 72.15 MPa, meaning the average absolute difference between predicted and actual values. Lastly, RMSE registered at 84.94 MPa, denoting the square root of the average of squared prediction errors.

As a reference, the observed experimental standard deviation for the grouped replicated trials was approximately 120.8 MPa (Table 4). Considering this value alongside the CI presented in Fig. 13, the values of MAE and RMSE fall within a reasonable and expected fluctuation for the assessment of the predicted RS.

In Eq. (11), it is presented the W matrix with the resulting values for the weights corresponding to each output from the hidden reference layer for the RBFN after training stage. The value for the hidden layer of bias neuron was B = 4.94575.

$$W = \begin{bmatrix} -3053.056167 \\ 1038.06034 \\ 217.683845 \\ -210.429561 \\ 867.885742 \\ 1139.880052 \end{bmatrix} \tag{11}$$

For visualization purposes, the regression expression obtained for the RS prediction was assembled, consisting of (m + 1) = 6 blocks, plus the bias parcel B. Eq. (12) presents the normalized version for the RBFN model, and Eq. (13) is the denormalize procedure to establish the RS predicted values in MPa. These equations can be used to check and compare the work results offline from the model, creating a simple validation method.

Eq. (12) and Eq. (13), due to their simplistic architectures, can be readily incorporated or encapsulated within intelligent measurement sensor modules (Smart Sensors), which can facilitate their integration and utilization within the production system. Incorporating intelligence into smart sensors enables a more efficient and effective process of data collection, analysis, and response when compared to conventional sensors, [65,66].

$$\begin{aligned} RS_{norm} = & -3053.056167 \cdot \sqrt{1 + 0.447214^2 \cdot \left((Vc)^2 + (f)^2 + (ap)^2 + (tp)^2 + (Fp)^2 \right)} \\ & + 1038.06034 \cdot \sqrt{1 + 0.447214^2 \cdot \left((Vc - 0.015498)^2 + (f + 0.273248)^2 + (ap + 0.531263)^2 + (tp + 0.351367)^2 + (Fp + 0.720692)^2 \right)} \\ & + 217.683845 \cdot \sqrt{1 + 0.447214^2 \cdot \left((Vc + 0.109007)^2 + (f - 0.616915)^2 + (ap + 0.615523)^2 + (tp + 0.477936)^2 + (Fp + 0.015522)^2 \right)} \\ & - 210.429561 \cdot \sqrt{1 + 0.447214^2 \cdot \left((Vc + 0.971071)^2 + (f - 0.070195)^2 + (ap - 0.074857)^2 + (tp - 0.215601)^2 + (Fp - 0.002437)^2 \right)} \\ & + 867.885742 \cdot \sqrt{1 + 0.447214^2 \cdot \left((Vc + 0.211753)^2 + (f + 0.670377)^2 + (ap + 0.08599)^2 + (tp + 0.705273)^2 + (Fp + 0.030843)^2 \right)} \\ & + 1139.880052 \cdot \sqrt{1 + 0.447214^2 \cdot \left((Vc - 0.007672)^2 + (f + 0.300697)^2 + (ap + 0.57087)^2 + (tp - 0.322838)^2 + (Fp - 0.692391)^2 \right)} \\ & + 4.945751 \end{aligned} \tag{12}$$

$$RS_{predicted} = RS_{norm} \cdot 796 - 892(MPa) \tag{13}$$

Generally, performance results obtained in the training stage tend to be biased since the training data (41 out of 59 tests) feed the calculation of the metrics in question. In this study, we chose to evaluate the model based on the 18 tests not used in the training stage; this way, we have a condition closer to the actual application of the model.

3.4. Testing stage performance

For the test/validation stage of the model, the following runs were used: # (5, 6, 8, 15, 18, 22, 25, 26, 27, 34, 37, 38, 39, 42, 51, 52, 56, 59). Fig. 14 compares the results obtained during the testing phase with the 18 randomly selected trials, which were not included in the training dataset. From Fig. 14, it is possible to notice that there is also an agreement between the ML estimate (red dash line) and the experimental points (continuous line) for the testing stage. The PCA-RBFN model appeared to have the capacity to predict the value of the RS from new measurements of the five established input factors from

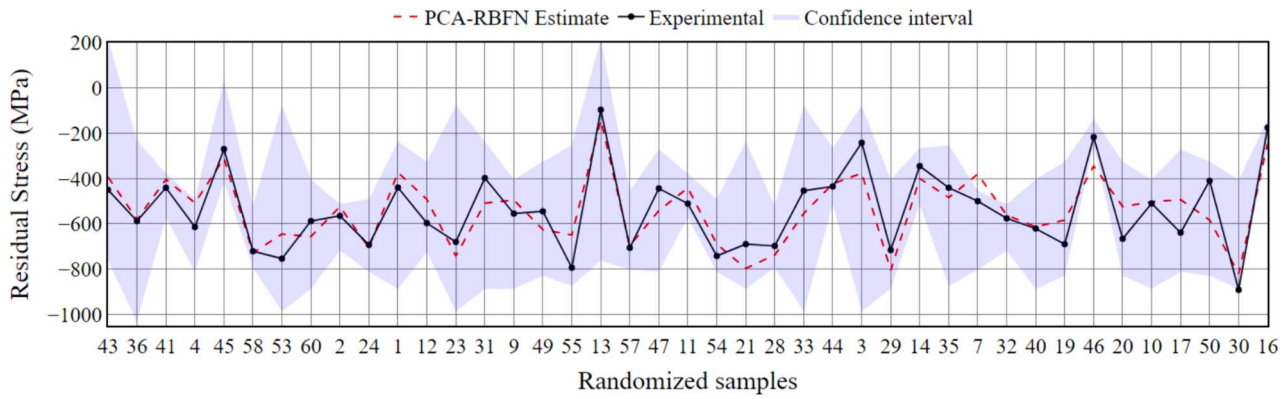

Fig. 13. Comparison of results for the PCA-RBFN training stage.

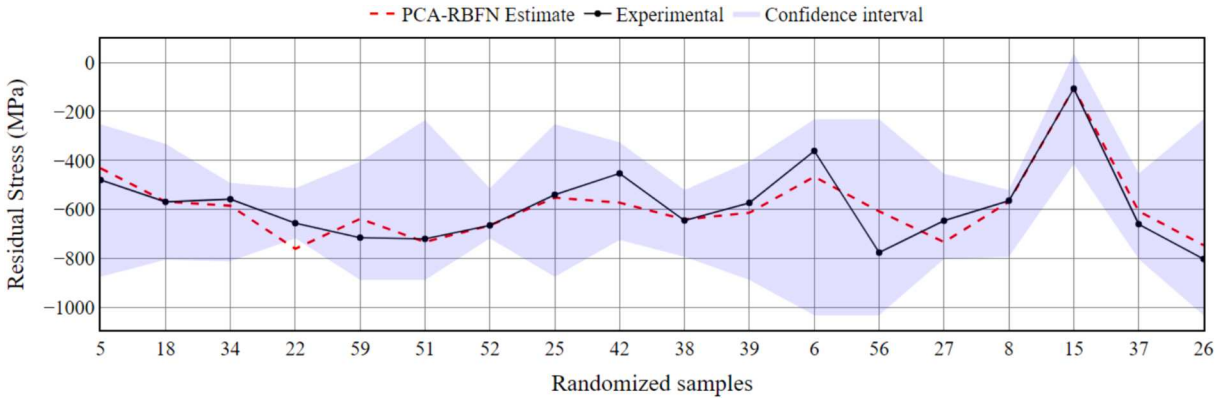

Fig. 14. Comparison of results for the ML PCA-RBFN testing stage.

Table 8. Additionally, alongside the experimental data points and the PCA-RBFN estimate, the 95 % confidence interval (CI) is presented and calculated based on the experimental values. As per Fig. 14, only one estimate falls slightly outside the 95 % confidence interval (CI), sample #22. All the remaining estimates are within the interval.

As performed in the training phase, performance in the model testing stage was evaluated using the same metrics used in the testing phase to enable comparative evaluation between the two stages, Table 9.

The evaluation metrics for this phase revealed the model's performance near real application conditions. The coefficient of determination R2 achieved a value of 80.54 %, indicative of the model's ability to account for 80.54 % of the variance in the data. The $R2_{adj}$ was calculated at 72.44 %, providing a measure considering the complexity of the number of predictors in the model. The MAE was determined to be 51.25 MPa, signifying the average absolute difference between predicted and actual values. RMSE was 70.36 MPa, reflecting the square root of the average squared prediction errors. The observed experimental standard deviation for the grouped replicated testing stage trials was approximately 77 MPa. Considering this value alongside the CI presented in Fig. 13, the values of MEA and RMSE fall within a reasonable and expected fluctuation for the assessment of the predicted RS in the testing stage.

Table 9
Comparative evaluation between the two stages.

	Training stage	Test stage	
R^2	76.66	80.54	%
R^2_{adj}	73.32	72.44	%
R^2_{pred}	69.37	–	%
MAE	72.15	51.25	MPa
RMSE	84.94	70.36	MPa

The comparison of performance metrics between the training and testing stages, as presented in Table 9, reveals coherence in results for the model. An important metric in this study is the R^2_{adj}, which assesses performance while considering the number of input factors involved in the model or the model's complexity.

An exception should be noted for R^2_{pred}, which only holds relevance for the training stage. R^2_{pred} is calculated using the leave-one-out cross-validation (LOOCV) methodology [64] to approximate the model's predictive ability during the training stage. Given that $R2_{pred}$ establishes a criterion for evaluating untrained data, it becomes possible to draw a parallel between the R^2_{pred} of the training stage and the R^2_{adj} of the testing stage, where all data were not used for the machine learning modeling. In this regard, the model's predictive capability is affirmed, as both values were close (with a difference of approximately 3 %).

While the MAE and RMSE values decreased during the testing phase, it is important to approach their assessment cautiously. Consideration should be given to the specific values used in the testing process, which were randomly selected by the routine and might have contributed to a reduced dispersion of the absolute error. The metrics MAE and RMSE, as outlined by Elsheikh [30], are closely linked to the data and outcomes assessed in the final applications post-model implementation. This is due to their intuitive interpretation, keeping the same units as the values analyzed. The volatile nature of residual stress is a highly relevant phenomenon in various engineering fields, particularly in the manufacturing and construction industries. These metrics provide a more easily comprehensible perspective when evaluating the model's practical application results [29].

Bar plots of the predicted versus the actual values are an efficient way to visualize the data and observe the model's performance. Fig. 15 compares the absolute RS results obtained during the testing phase with the 18 randomly selected trials, which were not included in the training

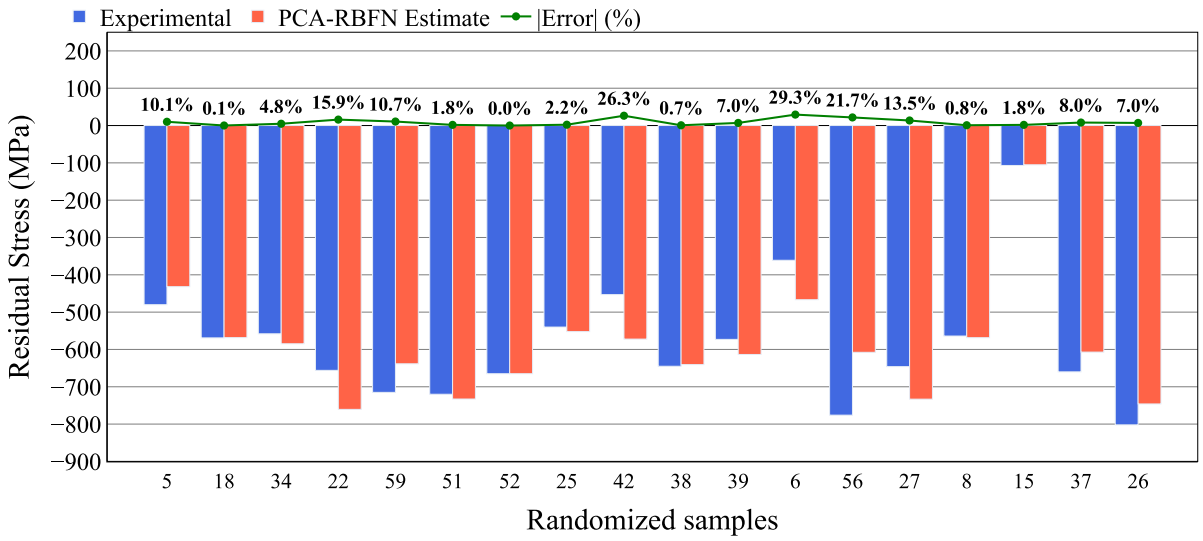

Fig. 15. Absolute error comparison of ML PCA-RBF-N testing stage results.

dataset.

The blue bar represents the actual value of RS in MPa measured during the experimental stage, while the red bar indicates the outcome obtained using the PCA-RBFN algorithm. Alongside these two results, the percentage error in absolute form is presented for each of the 18 trials. The highest absolute percentage error occurred in the sample resulting from run #6, at 29.3 %. For sample #52, the model exhibited a response very close to the actual value, with an error percentage of 0.0 %, considering one decimal place in the analysis. On average, the PCA-RBFN model demonstrated an absolute percentage error of approximately 9.0 %. This metric is the mean absolute percentage error (MAPE) [30]. As a percentage, this metric becomes highly intuitive for both developer interpretation and communication of results with individuals lacking technical expertise.

An important aspect in the estimated results is that there was no error in the direction of RS; all results showed compressive RS values consistent with the experimental values. There was no induction of false positives, which would likely create a condition of a positive tensile RS as an estimate. In a production system, this result would lead to the segregation of this part as scrap, as positive tensile RS is generally undesirable on the surface of machined components, [14].

Similar results in terms of performance determination were observed by Wittich et al. [48], who employed the least absolute shrinkage and selection operator (LASSO) and stepwise regression (SWR) in their investigation of empirical modeling of residual stress (RS) profiles in hard turning. The results obtained in terms of MAE and RMSE align with the range of variation observed in various measurement methods [61,62,67].

4. PCA-RBFN method performance comparison

In the manufacturing industry, the potential integration of predictive models into machine controllers or sensors, enabling automated quality control and traceability techniques, depends upon the ability to provide these control systems with a robust yet computationally lightweight methodology. This is essential due to potential processing limitations inherent in the hardware used in industrial equipment.

The control system of industrial manufacturing equipment is intricately linked with the regular operations of the manufacturing apparatus. This involves the control of actuators and other essential routines necessary for the proper functioning of the equipment during manufacturing processes. As a result, there is a limitation on the utilization of the system control resources for predictive control, as it can potentially overload the system.

Table 10
Summary metrics for different methods for RBFN modeling.

	scenario 1	scenario 2	units
# factors	8	5	
centroids	stochastically	PCA-eigenvectors	
training stage			
Iterations	221,923	3	cycles
R^2	82.03	76.66	%
R^2_{adj}	77.53	73.32	%
R^2_{pred}	72.56	69.37	%
MAE	59.83	72.15	MPa
RMSE	75.16	84.94	MPa
test stage			
R^2	71.83	80.54	%
R^2_{adj}	46.78	72.44	%
MAE	73.15	51.25	MPa
RMSE	88.48	70.36	MPa
MAPE	14.77	8.99	%

Another issue is the availability of real-time prediction during the processing of the manufacturing process or the response time of the prediction method. An important aspect of this approach (PCA-RBFN) is that the proposal allows for the implementation of an adaptive mode to the learning algorithm model in an online manner within production systems. The response's processing speed is a fundamental factor influencing equipment decision-making. Delayed decision-making could lead to reduced productivity or manufacturing defective parts, such as RS outside the desired compression condition.

To evaluate the efficiency of the methodology proposed in this study, a comparison was conducted between a stochastic (or conventional) method of modeling RBFN involving trial-and-error iterations on randomly selected values within an objective minimizing function and the PCA-RBFN method. This comparison aimed to assess the computational effort required to achieve a satisfactory predictive performance for RS in MPa using the same datasets (training and test). To quantify the computational effort, the selected metric for evaluation was the count of iterations required to determine centroid values for the RBFN hidden layer units. For the stochastic RBFN method, the objective function aimed at minimizing the MAE with stopping conditions set at a reduction rate over iterations <0.001 and a difference between consecutive

MAE values $\leq$ 0.5 %.

The results of the metric analysis for various model approaches are presented in Table 10, organized into two distinct scenarios. The first scenario, labeled as Scenario 1, uses all the original eight factors derived from the experimental dataset without any prior dimensionality reduction. In this scenario, the centroids for the hidden layer units were defined stochastically. The second scenario, Scenario 2, involved the PCA routine for dimension reduction and centroids valuation, according to the methodology in Fig. 11.

For each scenario, all metrics were determined, allowing one to assess the impact of different training approaches. The factors considered in Table 10 analysis were V_C, f, a_P, r_ε, type, F_f, F_C, and F_P for Scenario 1 and V_C, f, a_P, type, and F_P (after PCA dimensional reduction) for Scenario 2. The stochastic modeling approach in Scenario 1 presented a significant disadvantage due to the substantial number of iterations required to achieve a satisfactory metric outcome.

This increased number of iterations resulted from the methodology employed, which aimed to identify the optimal centroid combinations that minimize MAE. It took 221,923 iterations to meet the stopping conditions. Depending on the hardware involved in the industrial control system, the time taken to iterate through this quantity of times can range from several tens of seconds to minutes. This is not reasonable in terms of productivity for real-time control purposes. While this approach produced better metrics for training, including a R^2_{adj} of 77.53 % and a relatively lower MAE of 59.83 MPa, it exhibited signs of overfitting, a common concern in machine learning models when it demonstrates strong performance on trained data but faces limitations in generalizing to unseen data. This issue was evident in the considerable drop in performance during the test stage, where the R^2_{adj} decreased to 46.78 % and the MAE surged to 73.15 MPa.

These disparities between training and test stage metrics indicate the model's inability to generalize well to new data, emphasizing the limitation of this methodology. In contrast, Scenario 2 showcased significantly lower computational complexity, requiring a mere three iterations during the training stage. Despite this reduction in complexity, Scenario 2 exhibited competitive metrics to Scenario 1, boasting an $R2_{adj}$ of 73.32 % during the training stage and demonstrating improved generalization ability during the test stage, with an R^2_{adj} reaching 77.44 % and a reduced MAE of 51.25 MPa. This approach presented a notable mitigation of overfitting concerns, as evidenced by the narrower gap between the performance in the training and test stages, indicating improved adaptability to new data while maintaining computational efficiency.

In Table 10 although the training stage for Scenario 1 presented better metrics, despite the number of iterations, the test stage analysis reveals that, for the testing scenarios, the use of the PCA approach model consistently demonstrates better performance, fit, and generalization ability, compared to the conventional RBFN approach.

5. Conclusions

This study introduced a systematic method for monitoring and predicting RS during machining processes, providing a comprehensive approach for real-time predictive evaluations. A ML model was successfully developed using PCA for dimensionality reduction and RBFN for RS prediction. PCA reduced the initial eight factors to five principal components, and the hybrid PCA-RBFN model, utilizing a multiquadric radial function, showed strong performance in both the training and testing stages.

Performance metrics confirmed the model's predictive capabilities, with R2 (76.66 %), $R2_{adj}$ (73.32 %), R^2_{pred} (69.37 %), MAE (72.15 MPa), and RMSE (84.94 MPa) during training, and R^2 (80.54 %), R^2_{adj} (72.44 %), MAE (51.25 MPa), and RMSE (70.36 MPa) during testing stage. This consistency demonstrates the model's ability to generalize well to new data.

A comparative analysis with a stochastic RBFN method revealed the PCA-RBFN model's superior generalization ability, avoiding overfitting and yielding reliable predictions with fewer iterations.

The PCA-RBFN methodology has practical implications for the manufacturing industry by enabling the integration of lightweight predictive models into machine controllers or sensors. Two integration approaches are proposed: (i) direct incorporation of a pre-trained model into machining force measurement sensors for prompt decision-making and (ii) seamless integration of an adaptive learning algorithm into production systems for continuous real-time adjustments, enhancing efficiency and accuracy.

The generalization capability of this approach suggests its potential applicability in diverse industrial settings, enabling the adaptation of the model to various machining processes and materials. Future research could explore these possibilities, further validating the robustness and versatility of the PCA-RBFN model across different contexts.

Future research could analyze the strengths and weaknesses of the hybrid PCA-RBFN method by comparing it with other advanced machine learning approaches, such as convolutional and recurrent neural networks (CNN and RNN) and neural networks with backpropagation. This could reveal the performance of PCA-RBFN relative to more complex architectures. Additionally, support vector machines (SVM), known for their robustness in high-dimensional spaces, could be a useful benchmark, especially with kernel techniques like RBF. Other hybrid approaches could also be considered, like combining PCA with SVM or using genetic algorithms for centroid optimization in RBFN.

6. Declaration of Generative AI and AI-assisted technologies in the writing process

The authors affirm their use of generative AI and AI-assisted technologies throughout the manuscript development process. Specifically, the authors used Grammarly® to improve the English text. After using this tool, the authors reviewed and edited the content as needed, and they take full responsibility for the publication's content.

7. Ethics statement

The authors affirm that they have carefully reviewed and adhered to the ethical guidelines for publication. Furthermore, they confirm that the present study does not involve human subjects, animal experimentation, or the utilization of data sourced from social media platforms.

CRediT authorship contribution statement

Adalto Farias: Writing – review & editing, Writing – original draft, Visualization, Software, Methodology, Formal analysis, Conceptualization. **Nelson W. Paschoalinoto:** Writing – review & editing, Investigation. **Ed C. Bordinassi:** Writing – review & editing, Investigation. **Fabrizio Leonardi:** Writing – review & editing, Writing – original draft, Validation. **Sérgio Delijaicov:** Writing – review & editing, Writing – original draft, Validation, Supervision, Methodology.

Declaration of competing interest

The authors declare that they have no known competing financial interests or personal relationships that could have appeared to influence the work reported in this paper.

Acknowledgments

This research received no specific grant from funding agencies in the public, commercial, or not-for-profit sectors.

References

[1] V. Alcácer, V. Cruz-Machado, Scanning the industry 4.0: A literature review on technologies for manufacturing systems, Eng. Sci. Technol. An Int. J. 22 (2019) 899–919.

[2] C. Li, Y. Chen, Y. Shang, A review of industrial big data for decision making in intelligent manufacturing, Eng. Sci. Technol. an Int. J. 29 (2022) 101021.

[3] A.M. Mazid, T. Imam, K.B. Ahsan, N. Khandoker, Characterising surface roughness of Ti-6Al-4V alloy machined using coated and uncoated carbide tools with variable nose radius by machine learning, Eng. Appl. Artif. Intell. 124 (2023) 106546.

[4] W. Rajhi, et al., A contribution to numerical prediction of surface damage and residual stresses on die-sinking EDM of Ti6Al4V, J. Manuf. Process. 68 (2021) 1458–1484.

[5] J. Weng, et al., An analytical method for continuously predicting mechanics and residual stress in fillet surface turning, J. Manuf. Process. 68 (2021) 1860–1879.

[6] M.A. Khan, S.H.I. Jaffery, M. Khan, Assessment of sustainability of machining Ti-6Al-4V under cryogenic condition using energy map approach, Eng. Sci. Technol. an Int. J. 41 (2023) 101357.

[7] N.W. Paschoalinoto, et al., MQL strategies applied in Ti-6Al-4V alloy milling-Comparative analysis between experimental design and artificial neural networks, Materials (Basel) 13 (2020).

[8] W. Akhtar, I. Lazoglu, S.Y. Liang, Prediction and control of residual stress-based distortions in the machining of aerospace parts: A review, J. Manuf. Process. 76 (2022) 106–122.

[9] A.B. Khoshaim, A.H. Elsheikh, E.B. Moustafa, M. Basha, A.O. Mosleh, Prediction of residual stresses in turning of pure iron using artificial intelligence-based methods, J. Mater. Res. Technol. 11 (2021) 2181–2194.

[10] P. Geng, et al., Prediction of residual stresses within dissimilar Al/steel friction stir lap welds using an Eulerian-based modeling approach, J. Manuf. Process. 79 (2022) 340–355.

[11] G. Li, W. Lu, S. Huang, X. Zhang, S. Ding, Analysis and prediction of residual stresses based on cutting temperature and cutting force in rough turning of Ti–6Al–4V, Heliyon 8 (2022) e11661.

[12] M. Meurer, B. Tekkaya, D. Schraknepper, T. Bergs, S. Münstermann, Numerical prediction of machining induced residual stresses when hard cutting AISI 4140, Procedia CIRP 108 (2022) 583–588.

[13] J. Mathew, J. Griffin, M. Alamaniotis, S. Kanarachos, M.E. Fitzpatrick, Prediction of welding residual stresses using machine learning: Comparison between neural networks and neuro-fuzzy systems, Appl. Soft Comput. J. 70 (2018) 131–146.

[14] A.H. Elsheikh, et al., Fine-tuned artificial intelligence model using pigeon optimizer for prediction of residual stresses during turning of Inconel 718, J. Mater. Res. Technol. 15 (2021) 3622–3634.

[15] Y. Rahul, J. Mathew, Methodology for prediction of sub-surface residual stress in micro end milling of Ti-6Al-4V alloy, J. Manuf. Process. 62 (2021) 600–612.

[16] C. Schott, F. Wittich, A. Kroll, T. Niendorf, Prediction of near surface residual stress states for hard turned specimens using data driven nonlinear models, Procedia CIRP 101 (2021) 1–4.

[17] P.J. Arrazola, T. Özel, D. Umbrello, M. Davies, I.S. Jawahir, Recent advances in modelling of metal machining processes, CIRP Ann. - Manuf. Technol. 62 (2013) 695–718.

[18] M. Alamaniotis, J. Mathew, A. Chroneos, M.E. Fitzpatrick, L.H. Tsoukalas, Probabilistic kernel machines for predictive monitoring of weld residual stress in energy systems, Eng. Appl. Artif. Intell. 71 (2018) 138–154.

[19] C. Pati, A.K. Panda, A.K. Tripathy, S.K. Pradhan, S. Patnaik, A novel hybrid machine learning approach for change detection in remote sensing images, Eng. Sci. Technol. An Int. J. 23 (2020) 973–981.

[20] S. P. Leo Kumar, State of the art-intense review on artificial intelligence systems application in process planning and manufacturing. *Eng. Appl. Artif. Intell.* 65 (2017) 294–329.

[21] L. Zhang, J. Liu, C. Ma, H. Gui, Intelligent integrated framework towards high-accuracy machining, Eng. Sci. Technol. An Int. J. 40 (2023) 101359.

[22] A. Kukreja, S.S. Pande, Optimal toolpath planning strategy prediction using machine learning technique, Eng. Appl. Artif. Intell. 123 (2023) 106464.

[23] J. Rajaguru, M. Dwivedi, S. Natarajan, H. Krishnaswamy, N. Arunachalam, Machining induced residual stress prediction during orthogonal cutting of super duplex stainless steel using CEL approach, J. Manuf. Process. 82 (2022) 474–487.

[24] O. Sánchez-López, I. Hernández-Castillo, C.H. Castañeda-Roldán, A. Santiago-Alvarado, A.S. Cruz-Félix, Surface roughness modeling using response surface methodology and a variant of multiquadric radial basis function, Int. J. Adv. Manuf. Technol. 110 (2020) 3311–3322.

[25] N. Chu, W. Kang, X. Yao, J. Fu, Online roundness prediction of grinding workpiece based on vibration signals and support vector machine, Int. J. Adv. Manuf. Technol. 2733–2743 (2023), https://doi.org/10.1007/s00170-023-11206-6.

[26] T. Ghosh, K. Martinsen, Generalized approach for multi-response machining process optimization using machine learning and evolutionary algorithms, Eng. Sci. Technol. an Int. J. 23 (2020) 650–663.

[27] G.S. Schajer, M.B. Prime, P.J. Withers, Why is it so challenging to measure residual stresses? Exp. Mech. 62 (2022) 1521–1530.

[28] H.B. Motra, J. Hildebrand, A. Dimmig-Osburg, Assessment of strain measurement techniques to characterise mechanical properties of structural steel, Eng. Sci. Technol. an Int. J. 17 (2014) 260–269.

[29] S. Salmani Ghanbari, A.H. Mahmoudi, An improvement in data interpretation to estimate residual stresses and mechanical properties using instrumented indentation: A comparison between machine learning and Kriging model, Eng. Appl. Artif. Intell. 114 (2022) 105186.

[30] A.H. Elsheikh, Applications of machine learning in friction stir welding: Prediction of joint properties, real-time control and tool failure diagnosis, Eng. Appl. Artif. Intell. 121 (2023) 105961.

[31] J. Lin, R.J. Lian, Hybrid self-organizing fuzzy and radial basis-function neural-network controller for constant cutting force in turning, Int. J. Adv. Manuf. Technol. 53 (2011) 921–933.

[32] S. Samantaray, A. Sahoo, Prediction of flow discharge in Mahanadi River Basin, India, based on novel hybrid SVM approaches, Environ. Dev. Sustain. (2023).

[33] R.J. Praga-Alejo, D.S. González-González, M. Cantú-Sifuentes, L.M. Torres-Treviño, The ridge method in a radial basis function neural network, Int. J. Adv. Manuf. Technol. 79 (2015) 1787–1796.

[34] G. Fu, H. Gong, H. Gao, T. Gu, Z. Cao, Integrated thermal error modeling of machine tool spindle using a chicken swarm optimization algorithm-based radial basic function neural network, Int. J. Adv. Manuf. Technol. 105 (2019) 2039–2055.

[35] T.J. Li, T.Y. Sun, Y.M. Zhang, C.Y. Zhao, Prediction of thermal error for feed system of machine tools based on random radial basis function neural network, Int. J. Adv. Manuf. Technol. 114 (2021) 1545–1553.

[36] B. Ullah, W. Khan, Siraj-ul-Islam, Z. Ullah, A coupled meshless element-free Galerkin and radial basis functions method for level set-based topology optimization, J. Brazilian Soc. Mech. Sci. Eng. 44 (2022) 1–19.

[37] T. Banda, Y.C. Liu, A.A. Farid, C.S. Lim, A machine learning model for flank wear prediction in face milling of Inconel 718, Int. J. Adv. Manuf. Technol. 935–945 (2023), https://doi.org/10.1007/s00170-023-11152-3.

[38] P. Pai Srinivasa, T.N. Nagabhushana, P.K. Ramakrishna Rao, Flank wear estimation in face milling based on radial basis function neural networks, Int. J. Adv. Manuf. Technol. 20 (2002) 241–247.

[39] D.K. Sonar, U.S. Dixit, D.K. Ojha, The application of a radial basis function neural network for predicting the surface roughness in a turning process, Int. J. Adv. Manuf. Technol. 27 (2006) 661–666.

[40] C.C. Tsao, Comparison between response surface methodology and radial basis function network for core-center drill in drilling composite materials, Int. J. Adv. Manuf. Technol. 37 (2008) 1061–1068.

[41] H. Tao, et al., Hybridized artificial intelligence models with nature-inspired algorithms for river flow modeling: A comprehensive review, assessment, and possible future research directions, Eng. Appl. Artif. Intell. 129 (2024) 107559.

[42] B.O.P. Soepangkat, R. Norcahyo, M.K. Effendi, B. Pramujati, Multi-response optimization of carbon fiber reinforced polymer (CFRP) drilling using back propagation neural network-particle swarm optimization (BPNN-PSO), Eng. Sci. Technol. an Int. J. 23 (2020) 700–713.

[43] M.R. Phate, S.B. Toney, Modeling and prediction of WEDM performance parameters for Al/SiCp MMC using dimensional analysis and artificial neural network, Eng. Sci. Technol. An Int. J. 22 (2019) 468–476.

[44] L. Puggini, S. McLoone, An enhanced variable selection and Isolation Forest based methodology for anomaly detection with OES data, Eng. Appl. Artif. Intell. 67 (2018) 126–135.

[45] D. Garcia-Alvarez, A. Bregon, B. Pulido, C.J. Alonso-Gonzalez, Integrating PCA and structural model decomposition to improve fault monitoring and diagnosis with varying operation points, Eng. Appl. Artif. Intell. 122 (2023) 106145.

[46] H.F. Chen, et al., Predicting residual stress of aluminum nitride thin-film by incorporating manifold learning and tree-based ensemble classifier, Mater. Chem. Phys. 295 (2023) 127070.

[47] S. Samantaray, P. Sahoo, A. Sahoo, D.P. Satapathy, Flood discharge prediction using improved ANFIS model combined with hybrid particle swarm optimisation and slime mould algorithm, Environ. Sci. Pollut. Res. 30 (2023) 83845–83872.

[48] F. Wittich, M. Kahl, A. Kroll, W. Zinn, T. Niendorf, On nonlinear empirical modeling of residual stress profiles in hard turning, in: *2019 IEEE International Conference on Systems, Man and Cybernetics (SMC)* Vols 2019-Octob 3255–3260 (IEEE, 2019).

[49] A. Caggiano, R. Angelone, F. Napolitano, L. Nele, R. Teti, Dimensionality reduction of sensorial features by principal component analysis for ANN machine learning in tool condition monitoring of CFRP drilling, Procedia CIRP 78 (2018) 307–312.

[50] K. Stergiou, et al., Enhancing property prediction and process optimization in building materials through machine learning: A review, Comput. Mater. Sci. 220 (2023) 112031.

[51] A. de Farias, M.O. dos Santos, E.C. Bordinassi, Development of a thermal error compensation system for a CNC machine using a radial basis function neural network, J. Brazilian Soc. Mech. Sci. Eng. 44 (2022) 494.

[52] C.C. Aggarwal, Neural Networks and Deep Learning - A Textbook, Springer, Cham, 2018.

[53] J. Laurikkala, et al. Informal identification of outliers in medical data, in: *Fifth International Workshop on Intelligent Data Analysis in Medicine and Pharmacology* 20–24 (2000).

[54] D.L. Whaley, The Interquartile Range: Theory and Estimation, East Tennessee State University, 2005.

[55] C.S.K. Dash, A.K. Behera, S. Dehuri, A. Ghosh, An outliers detection and elimination framework in classification task of data mining, Decis. Anal. J. 6 (2023) 100164.

[56] A. Smiti, A critical overview of outlier detection methods, Comput. Sci. Rev. 38 (2020) 100306.

[57] H. Liu, D. Schraknepper, T. Bergs, Investigation of residual stresses and workpiece distortion during high-feed milling of slender stainless steel components, Procedia CIRP 108 (2022) 495–500.

[58] C.M. Bishop, Pattern recognition and machine learning, in: EAI/Springer Innovations in Communication and Computing, Springer-Verlag, 2006, p. 778.

[59] P.V. Sabique, G. Pasupathy, S. Ramachandran, G. Shanmugasundar, Investigating the influence of dimensionality reduction on force estimation in robotic-assisted surgery using recurrent and convolutional networks, Eng. Appl. Artif. Intell. 126 (2023) 107045.
[60] G. Yao, J. Duo, C.S. Chen, L.H. Shen, Implicit local radial basis function interpolations based on function values, Appl. Math. Comput. 265 (2015) 91–102.
[61] N. Gautam, S. Anand Kumar, P.R. Mondi, Evaluation methods for residual stress measurement in large components, Mater. Today Proc. 44 (2020) 4239–4244.
[62] A. Tabatabaeian, et al., Residual stress in engineering materials: A review, Adv. Eng. Mater. 24 (2022) 1–28.
[63] S. Samantaray, A. Sahoo, F. Baliarsingh, Groundwater level prediction using an improved SVR model integrated with hybrid particle swarm optimization and firefly algorithm, Clean. Water 1 (2024) 100003.
[64] Y. Pang, et al., Enhanced Kriging leave-one-out cross-validation in improving model estimation and optimization, Comput. Methods Appl. Mech. Eng. 414 (2023) 116194.
[65] D. Zhang, B. Wei, Smart sensors and devices in artificial intelligence, Sensors 20 (2020) 2–5.
[66] P. Łuczak, et al., Boosting intelligent data analysis in smart sensors by integrating knowledge and machine learning, Sensors 21 (2021).
[67] N.S. Rossini, M. Dassisti, K.Y. Benyounis, A.G. Olabi, Methods of measuring residual stresses in components, Mater. Des. 35 (2012) 572–588.